

A finite element model for coupled 3D transient electromagnetic and structural dynamics problems

Shu Guo · Somnath Ghosh

Received: 13 November 2013 / Accepted: 30 January 2014 / Published online: 21 February 2014
© Springer-Verlag Berlin Heidelberg 2014

Abstract This paper develops a framework for coupling transient electromagnetic (EM) and dynamic mechanical (ME) fields to predict the evolution of electrical and magnetic fields and their fluxes in a vibrating substrate undergoing finite deformation. To achieve coupling between fields the governing equations are solved in the time domain. A Lagrangian description is invoked, in which the coupling scheme maps Maxwell's equations from spatial to material coordinates in the reference configuration. Physical variables in the Maxwell's equations are written in terms of a scalar potential and vector potentials. Non-uniqueness in the reduced set of equations is overcome through the introduction of a gauge condition. Selected features of the code are validated using existing solutions in the literature, as well as comparison with results of simulations with commercial software. Subsequently, two coupled simulations featuring EM fields excited by steady-state and transient electric current source in dynamically vibrating conducting media are studied.

Keywords Coupled multiphysics · Dynamic finite deformation · Transient electromagnetic · Time-domain finite element method

1 Introduction

The recent times have seen a high interest in multifunctional structures that are governed by multiphysics principles such as mechanical and electromagnetic relations. These structures can be components of small unmanned airborne vehi-

cles (UAVs), active skins of aircraft, meta-materials for optical and communication systems etc. These devices can have multiple phases in the form of embedded conductors and/or reinforcing fibers in the matrix or substrate. Conductors can also serve as reinforcing phases for structural integrity and stability. Standard EM devices such as antennae and sensors have been traditionally based on stiff structures and are typically designed for transmission of EM waves alone without deformation considerations. In the recent years, flexible devices in energy, sensing, memory, and electromagnetics such as high mobility and stretchable electronics, elastomer-based EM devices, optical dielectric resonator antennas etc. are increasingly gaining importance [1,2]. In most of these devices the mechanical fields in the structure have significant effect on the EM signals. Discussions on utility and requirements of load-bearing antenna have been made in [3,4]. Load bearing antennae are subjected to mechanical vibrations, which have frequencies that are considerably different from those for the EM field. For piezoelectric devices, coupling between the fields happens naturally since the piezoelectric material is able to convert mechanical energy to electrical energy and vice-versa. Other examples of ME–EM coupling include electromagnetic forming (EMF), where EM forces are utilized to deform a solid body in the forming process. There is a need for robust, coupled multiphysics computational models and codes for meaningful design of multifunctional structures and devices.

Modeling the evolution of EM fields in a moving deformable media is a challenging problem. Only a limited number of coupled computational models are available in the literature. Finite element analysis of the EM problems for signal transmission in antennas has been mostly carried out in the frequency domain [5]. However, frequency domain computations are not suitable when coupled with finite deformation analysis. Novel descriptions of hp-adaptive finite elements

S. Guo · S. Ghosh (✉)
Department of Civil Engineering, Johns Hopkins University,
Baltimore, MD 21218, USA
e-mail: sghosh20@jhu.edu

Table 1 Comparison of a few commercial codes for multiphysics ME–EM simulations

Software	Capability	Limitations
ABAQUS	Linear piezoelectric analysis with deformation	Does not couple general EM fields with ME fields
COMSOL	Coupled low frequency EM field, radio frequency EM field using vector potentials with ME field	Does not fully couple transient EM and ME fields in time domain
ANSYS	Couples EM and structural problems through thermal field	Does not directly couple high frequency EM fields with large dynamical deformation

methods for EM problems have been developed in [6,7]. Various generalizations of the hp-adaptive finite element methods have been made for coupled multiphysics problems with mechanical fields in [8]. For multifunctionality, EM equations need to be solved in the reference configuration, thus requiring a strong coupling with the deformation field. Finite deformation analysis of piezoelectric composite materials, used in sensors and actuators, have been conducted in [9–11], mostly under quasi-static assumptions. In [12,13] the electromagnetic forming processes have been simulated with coupled mechanical and EM fields. An analytical treatment has been discussed in [14] for transformations of the Maxwell's equations in a moving medium, where effective EM fields due to deformation are derived. Multiphysics problems of charged particles due to EM forces and the near-field effects on particulate dynamics have been modeled in [15–18]. Recently a few of the multiphysics commercial codes have included coupled mechanical-electromagnetic or ME–EM analysis capabilities. Table 1 summarizes capabilities and limitations of some of these codes.

In the present paper, a generalized framework is developed for coupling transient electromagnetic and dynamic mechanical fields to predict the evolution of electrical and magnetic fields and their fluxes in a vibrating substrate undergoing finite deformation. A catalog of EM problems in deforming media can be solved with this framework, e.g. load bearing antennae and piezoelectric sensors. To achieve coupling between fields with disparate frequency ranges, the governing equations are solved in the time domain, as opposed to the frequency domain. Following methods developed in [10,19,20], a Lagrangian description is invoked, in which the coupling scheme maps Maxwell's equations from spatial to material coordinates in the reference configuration. Weak forms of the coupled transient EM and dynamic ME equations are generated in the reference configuration by applying the Euler-Lagrange stationary conditions [19], and the Galerkin's method is used for developing the FE equations. For an efficient solution process, physical variables in the Maxwell's equations are written in terms of a scalar potential and vector potentials. The process reduces the number of Maxwell's equations and associated field variables. Non-uniqueness in the solution of the reduced set of equations is

overcome through the introduction of a gauge condition in the FE formulations. The boundary conditions also need to be appropriately represented in terms of the potentials that do not represent physical variables.

This paper starts with a discussion on the governing equations for the transient EM problem in a finite deformation dynamical setting in Sect. 2. The weak forms and finite element implementation are developed in Sect. 3. Aspects of parallel implementation of the code are discussed in this section. Section 4 introduces numerical examples that are simulated with the coupled dynamic electromagnetic (ME–EM) model and code. Selected features of the code are validated using existing solutions in the literature, as well as comparison with results of simulations by commercial software and codes. Subsequently two coupled simulations, featuring EM fields excited by steady-state and time varying electric current source in dynamically vibrating conducting media, are conducted and studied. Results demonstrate the effectiveness of the proposed method.

2 Governing equations for the transient electromagnetic problem in a finite deformation dynamical setting

Evaluation of transient EM field variables in a deformable, conducting medium undergoing finite dynamic deformation requires a comprehensive solution approach that couples the EM and ME fields through their governing equations. The evolution of the EM field variables depends on the deformed configuration, as well as on the pointwise velocity distribution of the vibrating medium. The mechanical field variables, in turn, are subject to be affected by electromagnetically induced forces, e.g. the Lorentz force. In many practical applications, such as load-bearing antenna, the magnitude of the Lorentz force is negligible in comparison with the externally applied mechanical forces on the structure. In these cases, the explicit effect of EM field variables on the mechanical field, e.g. the deformation of the structure may be ignored. This reduces to a one-way coupling between the two fields, i.e. only the EM variables are affected by the deformation of the structure. Rather than solving a fully coupled system, a staggered solution approach may be pursued to couple

the dynamical response with the EM field in this work. The governing equations for the mechanical and electromagnetic problems are discussed next.

2.1 Governing equations for the finite deformation dynamics problem

The mechanical response of the conducting medium is modeled using governing equations for a hyperelastic material undergoing finite deformation under dynamic loading conditions. In a Lagrangian formulation, the reference configuration $\Omega_0(=\Omega(t_0))$ at a time t_0 is expressed in terms of the material coordinates X_I , $I = 1, 2, 3$, while the current configuration $\Omega(t)$ at time t is represented by the current coordinates x_i , $i = 1, 2, 3$. The deformation of the body is expressed using the single-valued mapping function $x_i = \varphi_i(X_J, t)$. Correspondingly, the Cartesian components of the displacement vector in the material coordinates are expressed as: $u_i(X_J, t) = x_i - \delta_{ij}X_J$. The constitutive relation for the hyperelastic material at finite strains is assumed to be neo-Hookean, for which the strain energy density function W is expressed in terms of kinematics variables as:

$$W = \frac{1}{2}\lambda(\ln J)^2 - \mu \ln J + \frac{1}{2}\mu (C_{II} - 3) \tag{1}$$

where λ and μ are Lamé constants, and $C_{IJ}(= \frac{\partial x_k}{\partial X_I} \frac{\partial x_k}{\partial X_J})$ is the right Cauchy-Green deformation tensor. The positive-valued Jacobian J , which determines admissible deformation mapping, is defined in terms of the deformation gradient tensor F_{iJ} as:

$$J = \det(F_{iJ}) > 0 \quad \text{where} \quad F_{iJ} = \frac{\partial x_i}{\partial X_J} \tag{2}$$

The stress–strain relation for finite strains is derived from the energy density expression in (1) as:

$$\begin{aligned} S_{IJ} &= J \frac{\partial X_J}{\partial x_m} \frac{\partial X_I}{\partial x_n} \sigma_{mn} \\ &= 2 \frac{\partial W}{\partial C_{IJ}} = \lambda \ln J C_{IJ}^{-1} + \mu(\delta_{IJ} - C_{IJ}^{-1}) \end{aligned} \tag{3}$$

where S_{IJ} and σ_{ij} are components of the second Piola–Kirchhoff and Cauchy stress tensors respectively. A second hyperelastic logarithmic stretch model [21] is also implemented in this work, where the strain energy density function is defined in terms of principal strain ε_m as:

$$W = \frac{1}{2}\lambda \sum_{m=1}^3 (\varepsilon_m)^2 + \mu \sum_{m=1}^3 (\varepsilon_m^2) \tag{4}$$

where $\varepsilon_m = \log(\lambda_m)$, λ_m being the square root of the principal values of C_{IJ} . The principal values τ_m of Kirchhoff

stress τ_{ij} are expressed in term of W as:

$$\tau_m = \frac{\partial W}{\partial \varepsilon_m} = \lambda \left(\sum_{m=1}^3 \varepsilon_m \right) + 2\mu\varepsilon_m \tag{5}$$

Finally from Eq. (5), the second Piola–Kirchhoff is obtained as

$$\begin{aligned} S_{IJ} &= \frac{\partial x_I}{\partial x_k} \tau_{kl} \frac{\partial x_J}{\partial x_l} \\ &= \frac{\partial x_I}{\partial x_k} \sum_m \left[\lambda \left(\sum_{m=1}^3 \varepsilon_m \right) + 2\mu\varepsilon_m \right] q_k^{(m)} q_l^{(m)} \frac{\partial x_J}{\partial x_l} \end{aligned} \tag{6}$$

where $q_i^{(m)}$ are direction cosines of principal direction m and component direction i .

The equilibrium equation in finite deformation theory is expressed as:

$$\frac{\partial P_{iJ}}{\partial X_J} + \rho_0 b_i = \rho_0 \ddot{u}_i \tag{7}$$

where $P_{iJ}(= \frac{\partial x_i}{\partial X_K} S_{KJ})$ is the first Piola–Kirchhoff stress, ρ_0 is the density in the reference configuration and b_i is the body force per unit mass.

2.2 Governing equations for the electromagnetic problem in current and reference configurations

The governing equations for the EM problem is based on the conventional Maxwell’s equations for a conducting medium. In the current configuration, these equations are expressed in terms of the current coordinates $x_i(t)$ as:

$$d_{i,i} = q_e \quad \text{Gauss’ law of electricity} \tag{8a}$$

$$b_{i,i} = 0 \quad \text{Gauss’ law of magnetism} \tag{8b}$$

$$\varepsilon_{ijk} e_{k,j} = -\frac{\partial b_i}{\partial t} \quad \text{Faraday’s law of magnetism} \tag{8c}$$

$$\varepsilon_{ijk} h_{k,j} = \frac{\partial d_i}{\partial t} + j_i^f \quad \text{Ampere’s law} \tag{8d}$$

Here d_i represents the Cartesian components of the electrical displacement field vector, q_e is the free charge density, b_i are the components of the magnetic induction field vector, e_i is the electric field, h_i is the magnetic field strength, and j_i^f is the free charge current defined as:

$$j_i^f \triangleq j_i^c + q_e \dot{x}_i. \tag{9}$$

where j_i^c is conducting current and ε_{ijk} is the Levi-Civita permutation symbol. The constitutive laws for an isotropic material in the current configuration, in the absence of magnetization and polarization, are given as:

$$d_i = \varepsilon e_i, \quad h_i = \frac{1}{\mu} b_i, \quad j_i^c = \sigma(e_i + \varepsilon_{ijk} \dot{x}_j b_k) \tag{10}$$

where the permittivity ε , permeability μ and conductivity σ are material constants.

For coupling with the set of mechanical field equations for the deforming medium, it is necessary to represent the Maxwell’s equations in a reference material configuration Ω_0 . The Lagrangian description in Sect. 2.1, provides a consistent platform for solving the coupled dynamic-EM problem. The transformation from current to reference configuration requires the flux derivative of any field vector V_i in terms of the local time derivatives as [22]:

$$V_i^* = \frac{\partial V_i}{\partial t} + V_{j,j} \dot{x}_i + (V_i \dot{x}_k - V_k \dot{x}_i)_{,k} \tag{11}$$

satisfying the integral form of the flux derivative relation:

$$\frac{d}{dt} \int_{\partial\Omega} V_i n_i ds = \int_{\partial\Omega} V_j^* n_j ds. \tag{12}$$

Here \dot{x}_i corresponds to the velocity field and $(\cdot)_{,i}$ corresponds to the spatial derivative. Derivation of the relation (11) utilizes the Nanson’s formula of surface area transformation between the current and the reference configurations, expressed as:

$$n_i ds = J X_{J,i} N_J dS \tag{13}$$

where $n_i ds$ and $N_J dS$ are differential area vectors, ds and dS are surface areas, and n_i and N_J are surface normals in the current and reference configurations respectively. The flux derivative of the electric displacement d_i is obtained from Eq. (11) as:

$$\frac{\partial d_i}{\partial t} = d_i^* - (d_i \dot{x}_k - d_k \dot{x}_i)_{,k} - d_{j,j} \dot{x}_i \tag{14}$$

Now

$$\begin{aligned} \varepsilon_{ijk} \frac{\partial}{\partial x_j} h_k &= \varepsilon_{ikj} \frac{\partial}{\partial x_k} h_j = -\varepsilon_{ijk} \frac{\partial}{\partial x_k} h_j \quad \text{and} \\ (d_i \dot{x}_k - d_k \dot{x}_i)_{,k} &= (\delta_{im} \delta_{kn} - \delta_{km} \delta_{in})(d_m \dot{x}_n)_{,k} \\ &= \varepsilon_{jik} \varepsilon_{jmn} (d_m \dot{x}_n)_{,k} \end{aligned} \tag{15}$$

Substituting Eq. (8a) and (14) in Eq. (8d) and rearranging indices yields the relation:

$$\varepsilon_{ikj} [h_j + \varepsilon_{jmn} (d_m \dot{x}_n)]_{,k} = d_i^* + j_i^f - q_e \dot{x}_i \tag{16}$$

where, the identity $\sum_{i=1}^3 \varepsilon_{ijk} \varepsilon_{imn} = \delta_{im} \delta_{kn} - \delta_{km} \delta_{in}$ is used. Equation (16) is transformed to the reference configuration by integrating it over an arbitrary surface area in the current configuration, applying the Kelvin–Stokes’ theorem, and mapping to the reference configuration using Eq. (13) to yield:

$$\begin{aligned} \oint_C [h_i + \varepsilon_{imn} (d_m \dot{x}_n)] x_{i,J} dX_J \\ = \int_{\partial\Omega_0} (d_j^* + j_j^f - q_e \dot{x}_j) J X_{I,j} N_I dS_0 \end{aligned} \tag{17}$$

where C corresponds to the contour line around the surface. The reference configuration electric displacement, magnetic field and free charge current in the conductor are defined in terms of those in the current configuration as:

$$D_I \triangleq J X_{I,j} d_j \tag{18a}$$

$$H_J \triangleq [h_i + \varepsilon_{imn} (d_m \dot{x}_n)] x_{i,J} \tag{18b}$$

$$J_I^c \triangleq J X_{I,j} j_j^c \tag{18c}$$

With these reference configuration field variables, Eq. (17) is reduced to the configuration-invariant relation:

$$\varepsilon_{IJK} H_{K,J} = \frac{d}{dt} D_I + J_I^c \tag{19}$$

The permutation operator ε_{IJK} in the reference configuration is related to ε_{ijk} as:

$$\begin{aligned} \varepsilon_{IJK} &= J^{-1} \varepsilon_{ijk} x_{i,I} x_{j,J} x_{k,K} \quad \text{or inversely} \\ \varepsilon_{ijk} &= J \varepsilon_{IJK} X_{I,i} X_{J,j} X_{K,k} \end{aligned} \tag{20}$$

In a similar manner, substituting b_i in Eq. (11) and using Eqs. (8b) and (8c) results in a relation between the magnetic induction field b_i and the electric field e_i as:

$$\varepsilon_{ijk} e_{k,j} = (b_i \dot{x}_k - b_k \dot{x}_i)_{,k} - b_i^* \quad \text{or} \tag{21a}$$

$$\varepsilon_{ijk} [e_j - \varepsilon_{jmn} (b_m \dot{x}_n)]_{,k} = -b_i^* \tag{21b}$$

Integrating Eq. (21b) over a surface area in the current configuration, applying the Kelvin–Stokes’ theorem, and subsequently transforming into the reference configuration yields:

$$\oint_C [e_j - \varepsilon_{jmn} (b_m \dot{x}_n)] x_{j,I} dX_I = - \int_{\partial\Omega_0} b_j^* J X_{J,i} N_J dS_0 \tag{22}$$

The electric and magnetic induction fields in the reference configuration are defined as:

$$E_I \triangleq [e_j - \varepsilon_{jmn} (b_m \dot{x}_n)] x_{j,I} \tag{23a}$$

$$B_J \triangleq J X_{J,i} b_i \tag{23b}$$

The Faraday’s Eq. (8c) in the reference configuration is then expressed as:

$$\varepsilon_{IJK} E_{K,J} = - \frac{d}{dt} B_I \tag{24}$$

For the Gauss’ law of electricity in Eq. (8a), the transformation is achieved by integrating over the volume and applying

the divergence theorem, along with the Nanson’s formula of surface transformation, to yield:

$$\int_{\partial\Omega} d_i n_i ds = \int_{\Omega} q_e dv \Rightarrow \int_{\partial\Omega_0} d_i J X_{J,i} N_J dS = \int_{\Omega_0} q_e J dV \tag{25}$$

By defining the charge density in the reference configuration as $Q_e = J q_e$, Eq. (8a) in the reference configuration becomes

$$D_{I,I} = Q_e \tag{26}$$

Following the same mapping procedure, the Gauss’ law of magnetism of Eq. (8b) is transformed to:

$$B_{J,J} = 0 \tag{27}$$

In summary, the four Maxwell’s equations in the reference configuration are written in the indicial and vector forms as:

<u>Indicial Notations</u>	<u>Vector Notations</u>	
$D_{I,I} = Q_e$	$\nabla_X \cdot \mathbf{D} = Q_e$	(28)
$B_{J,J} = 0$	$\nabla_X \cdot \mathbf{B} = 0$	(29)

$\varepsilon_{IJK} \frac{\partial}{\partial X_J} E_K = -\frac{d}{dt} B_I$	$\nabla_X \times \mathbf{E} = -\frac{d}{dt} \mathbf{B}$	(30)
---	---	------

$\varepsilon_{IJK} \frac{\partial}{\partial X_J} H_K = \frac{d}{dt} D_I + J_I^c$	$\nabla_X \times \mathbf{H} = \frac{d}{dt} \mathbf{D} + \mathbf{J}^c$	(31)
--	---	------

Constitutive relations in the reference configuration, relating D_I and E_I , B_I and H_I , as well as J_I^c and E_I and B_I , are nonlinear due to coupling with the deformation fields. The following steps are used to determine the set of constitutive relations. Using the inverse of Eq. (23b), i.e.

$$b_j = J^{-1} x_{j,I} B_I \tag{32}$$

and the velocity relations

$$\dot{x}_i = -x_{i,K} \frac{\partial X_K}{\partial t} \text{ or inversely } \frac{\partial X_K}{\partial t} = -X_{K,i} \dot{x}_i \tag{33}$$

in Eq. (23a), its inverse is obtained as:

$$\begin{aligned} e_i &= E_J X_{J,i} + \varepsilon_{imn} (b_m \dot{x}_n) = E_J X_{J,i} \\ &\quad - X_{J,i} (\varepsilon_{imn} J^{-1} x_{i,J} x_{m,L} x_{n,K}) \left(\frac{\partial X_K}{\partial t} B_L \right) \\ &= X_{J,i} \left[E_J + \varepsilon_{JKL} \left(\frac{\partial X_K}{\partial t} B_L \right) \right] \end{aligned} \tag{34}$$

Substituting Eqs. (18a) and (10) in Eq. (34) yields the constitutive relation for the electrical displacement field in the

reference configuration as:

$$\begin{aligned} D_I &= \varepsilon J X_{I,j} X_{J,j} \left[E_J + \varepsilon_{JKL} \left(\frac{\partial X_K}{\partial t} B_L \right) \right] \\ &= \varepsilon J C_{IJ}^{-1} \left[E_J + \varepsilon_{JKL} \left(\frac{\partial X_K}{\partial t} B_L \right) \right] \end{aligned} \tag{35}$$

In a similar manner, the magnetic field strength in both configurations are related as:

$$\begin{aligned} h_i &= H_J X_{J,i} - \varepsilon_{imn} (d_m \dot{x}_n) = H_J X_{J,i} \\ &\quad + X_{J,i} (\varepsilon_{imn} J^{-1} x_{i,J} x_{m,L} x_{n,K}) \left(\frac{\partial X_K}{\partial t} D_L \right) \\ &= X_{J,i} \left[H_J - \left(\varepsilon_{JKL} \left(\frac{\partial X_K}{\partial t} D_L \right) \right) \right] \end{aligned} \tag{36}$$

Substituting Eqs. (32) and (35) in Eq. (36) results in the constitutive relation for magnetic field strength in the reference configuration as:

$$\begin{aligned} H_J &= h_i x_{i,J} + \varepsilon_{JKL} \frac{\partial X_K}{\partial t} D_L = \frac{1}{\mu} J^{-1} x_{i,M} x_{i,J} B_M \\ &\quad + \varepsilon_{JKL} \frac{\partial X_K}{\partial t} \left\{ \varepsilon J C_{LN}^{-1} \left[E_N + \varepsilon_{NPQ} \left(\frac{\partial X_P}{\partial t} B_Q \right) \right] \right\} \\ &= \frac{1}{\mu} J^{-1} C_{MJ} B_M + \varepsilon_{JKL} \frac{\partial X_K}{\partial t} \left\{ \varepsilon J C_{LN}^{-1} \left[E_N \right. \right. \\ &\quad \left. \left. + \varepsilon_{NPQ} \left(\frac{\partial X_P}{\partial t} B_Q \right) \right] \right\} \end{aligned} \tag{37}$$

Finally, incorporating Eq. (18c) and Eq. (34) in Eq. (10) provides the constitutive relation for the current in the reference configuration as:

$$J_I^c = \sigma J C_{IJ}^{-1} E_J \tag{38}$$

2.3 Scalar and vector potentials in current and reference configurations

For effective solution of the Maxwell’s equations, a scalar potential φ for the electric field and a vector potential \mathbf{a} for the magnetic field in the current configuration have been proposed as primary variables, e.g. in [22]. This representation in terms of the potential functions reduce the Maxwell’s equations from four to two independent equations. Since the divergence of the magnetic induction vector \mathbf{b} (in Eq. (8c)) is zero, the magnetic vector potential \mathbf{a} can be derived using a vector identity, i.e.

$$\nabla \cdot \mathbf{b} = \nabla \cdot (\nabla \times \mathbf{a}) = 0 \implies b_i = \varepsilon_{ijk} a_{k,j} \tag{39}$$

The Faraday’s law in Eq. (8c) may be rewritten in terms of the vector potential a_i by substituting the expression for the magnetic field b_i in Eq. (39), i.e.

$$\varepsilon_{ijk} (e_k + \dot{a}_k)_{,j} = 0 \tag{40}$$

Since the curl of the gradient of any scalar field is a null vector, the gradient of φ may be added to the LHS of Eq. (40) without changing the RHS, i.e.

$$\varepsilon_{ijk}(e_k + \dot{a}_k + \varphi_{,k}),_j = 0 \quad (41)$$

The electric field may be then be expressed using mixed potentials as:

$$e_k = -\varphi_{,k} - \dot{a}_k \quad (42)$$

For electrostatic problems, the electric potential φ corresponds to the ratio of potential energy to charge. Introduction of these two potentials in the Gauss's law for magnetism in Eq. (8b) and the Faraday's law in Eq. (8c) results in identities. The other two Maxwell's equations are reformulated using the mixed potentials as:

$$\nabla^2 \varphi + \frac{\partial}{\partial t}(a_{i,i}) = -q_e \quad (43a)$$

$$\left(\nabla^2 a_i - \mu \varepsilon \frac{\partial^2 a_i}{\partial t^2} \right) - \left(a_{k,k} + \mu \varepsilon \frac{\partial \varphi}{\partial t} \right)_{,i} = -\mu j_i \quad (43b)$$

The corresponding reduced forms of the Maxwell's equations in the reference configuration requires consistent forms of both the potentials in this configuration. Defining transformation functions as:

$$A_K = a_i x_{i,K} \iff a_i = A_K X_{K,i} \quad \text{and} \quad (44a)$$

$$\Phi = \varphi - \frac{dx_i}{dt} a_i \iff \varphi = \Phi - \frac{\partial X_I}{\partial t} A_I \quad (44b)$$

Scalar and vector potentials defined in the reference configuration follow relations similar to those in the current configuration, i.e.

$$E_I = -\Phi_{,I} - \frac{\partial A_I}{\partial t} \quad (45a)$$

$$B_I = \varepsilon_{IJK} A_{K,J} \quad (45b)$$

Details of the derivation of Eqs. (44a), (44b) and proofs of Eqs. (45a) and (45b) are given in [22]. Substituting Eqs. (45a) and (45b) in Eq. (28) and Eq. (31) results in the two governing equations

$$\left(\varepsilon J C_{IJ}^{-1} \tilde{E}_J \right)_{,I} = Q_e \quad (46a)$$

$$\begin{aligned} \varepsilon_{IJK} \left(\frac{1}{\mu J} C_{KLELMN} A_{N,M} + \varepsilon_{K PQ} \frac{\partial X_P}{\partial t} \varepsilon J C_{QR}^{-1} \tilde{E}_R \right)_{,J} \\ = \frac{d}{dt} \varepsilon J C_{IP}^{-1} \tilde{E}_P + \sigma J C_{IQ}^{-1} (-\Phi_{,Q} - \dot{A}_Q) \end{aligned} \quad (46b)$$

where \tilde{E}_I is defined as:

$$\begin{aligned} \tilde{E}_I &= E_I + \varepsilon_{IJK} \frac{\partial X_J}{\partial t} B_K \\ &= -\Phi_{,I} - \dot{A}_I + \varepsilon_{IJK} \frac{\partial X_J}{\partial t} \varepsilon_{KMN} A_{N,M} \end{aligned} \quad (47)$$

2.4 Constraint Gauge condition for solution uniqueness

While the reduced representation of Maxwell's equations in terms of potentials is computationally advantageous, the solution leads to non-uniqueness of the potentials and consequent singular tangent matrices for certain state of the EM fields. For example, the vector potential relation in Eq. (45b), can admit multiple solutions of the magnetic field due to the condition:

$$\nabla \cdot \mathbf{B} = \nabla \cdot (\nabla \times \mathbf{A} + \nabla \Psi) = 0 \implies B_I = \varepsilon_{IJK} A_{K,J} + \psi_{,I} \quad (48)$$

where A_I is the vector potential component and Ψ is any arbitrary scalar potential in the reference configuration. This non-uniqueness will lead to a singular tangent stiffness matrix and consequent instability in the finite element model. This has been averted through the introduction of a variety of constraint gauge conditions in the literature, viz. [11, 23–26]. The Coulomb gauge condition proposed in [11, 24, 26] is utilized in the present work. It is stated as:

$$A_{I,I} = 0 \quad (49)$$

This constraint forces the divergence of the vector potential \mathbf{A} to be zero. From the Helmholtz theorem [11], the vector potential \mathbf{A} can be decomposed into a divergence free rotational term and a curl-free irrotational term. Due to the vanishing irrotational part in Eq. (45b), the rotational term contributes to the magnetic field B_I and hence the Coulomb gauge implies a restriction to the irrotational term. The constraint gauge condition is implemented in the finite element in a weak sense, using the penalty formulation following [11, 24, 26].

3 Weak forms and finite element implementation

Weak forms of the Lagrangian FEM formulation in the reference configuration and their algorithmic implementation are discussed in this section. The principle of virtual work is used to obtain the weak form of the finite deformation dynamics problem in Eq. (7). The Hamilton's principle of stationary action, in conjunction with the penalty formulation of the gauge constraint condition, is used to develop the weak form of the time dependent EM field. Appropriate boundary conditions are developed for both the mechanical and electromagnetic problems in the reference configuration. The EM fields in the conducting medium are affected by the deformation and other mechanical field variables, while the EM fields have negligible effect on the mechanical fields in comparison with the external loading. Hence, the Lorentz force

is assumed to be negligible in this study. A one-directional coupling from the mechanical field to the EM field is thus considered, and a staggered solution scheme is implemented. A high performance parallel implementation of the coupled code is also summarized in this section.

3.1 Weak form and boundary conditions of the finite deformation dynamics problem

The principle of virtual work is developed by taking the inner product of Eq. (7) with the virtual displacement δu_i and integrating over volume in the reference configuration Ω_0 as:

$$\int_{\Omega_0} \delta u_i \frac{\partial P_{iJ}}{\partial X_J} dV_0 + \int_{\Omega_0} \delta u_i \rho_0 b_i dV_0 = \int_{\Omega_0} \delta u_i \rho_0 \ddot{u}_i dV_0 \quad (50)$$

By applying the divergence theorem together with integration by parts, the weak form reduces to

$$\begin{aligned} &\int_{\Omega_0} \delta u_i \rho_0 \ddot{u}_i dV_0 + \int_{\Omega_0} \delta F_{iJ} P_{iJ} dV_0 - \int_{\Omega_0} \delta u_i \rho_0 b_i dV_0 \\ &- \int_{\partial\Omega_0} \delta u_i P_{iJ} N_J dS_0 = 0 \end{aligned} \quad (51)$$

Displacement and traction conditions on respective boundaries in the reference configuration are expressed as:

$$\begin{aligned} U_I &= \delta_{Ii} u_i = \bar{U}_I^0 \quad \text{on } \Gamma_u \in \partial\Omega_0 \\ T_I &= P_{iJ} N_J = \bar{T}_I^0 \quad \text{on } \Gamma_t \in \partial\Omega_0 \end{aligned} \quad (52)$$

Since the EM fields are assumed to have negligible effect on the mechanical fields, the discrete form of Eq. (51), together with the boundary conditions Eq. (52), are sufficient for solving the deformation related fields of the substrate.

3.2 Weak form of the electromagnetic problem in the reference configuration

The weak form of the transient EM problem is derived using the Hamilton’s principle, [19,22]. It involves minimization of the action functional S over the time range $t_1 - t_2$, defined in terms of the time-dependent Lagrangian density \mathcal{L} in the reference domain, expressed as:

$$\delta S = \delta \int_{t_1}^{t_2} \int_{\Omega_0} \mathcal{L} d\Omega_0 dt = 0 \quad (53)$$

where the Lagrangian density in the reference and current configurations, \mathcal{L} and l respectively, are given as:

$$\mathcal{L} = J l = \left(\frac{\varepsilon}{2} e_i e_i - \frac{1}{2\mu} b_j b_j + j_k a_k - q\varphi \right) \quad (54)$$

\mathcal{L} may be expressed in terms of the scalar and vector potentials in the reference configuration using the expressions for e_i and b_i in Eqs. (34) and (32), and substituting Eqs. (44a) and (44b) as:

$$\mathcal{L} = \frac{\varepsilon J}{2} C_{JK}^{-1} \tilde{E}_J \tilde{E}_K - \frac{J^{-1}}{2\mu} (C_{LM} B_L B_M) + J_N A_N - Q\Phi \quad (55)$$

Here E_I , B_I and \tilde{E}_I are in terms of the scalar and vector potentials as given in Eqs. (45a), (45b) and (47).

Furthermore, the gauge condition in Eq. (49) is implemented using the penalty method to constrain the vector potentials following [11,24,26]. In this process, an additional term $\frac{1}{p}(\nabla \cdot \mathbf{A})^2$ is added to the Lagrangian density function as:

$$\begin{aligned} \mathcal{L} &= \frac{\varepsilon J}{2} C_{JK}^{-1} \tilde{E}_J \tilde{E}_K - \frac{J^{-1}}{2\mu} (C_{LM} B_L B_M) \\ &+ J_N A_N - Q\Phi + \frac{1}{p} (A_{P,P})^2 \end{aligned} \quad (56)$$

The term $\frac{1}{p}$ is the penalty coefficient, for which p is generally of the order of the electric permittivity ε .

From Eq. (53), setting the variation of the action functional S with respect to Φ and \mathbf{A} to zero yields:

$$S_{,\Phi} [\delta\Phi] = \int_{t_1}^{t_2} \int_{\Omega_0} \mathcal{L}_{,\Phi} [\delta\Phi] \Omega_0 dt = 0 \quad (57a)$$

$$S_{,\mathbf{A}} [\delta\mathbf{A}] = \int_{t_1}^{t_2} \int_{\Omega_0} \mathcal{L}_{,\mathbf{A}} [\delta\mathbf{A}] \Omega_0 dt = 0 \quad (57b)$$

Since t_1 and t_2 are arbitrary, Eqs. (57a) and (57b) lead to:

$$\begin{aligned} \int_{\Omega_0} \mathcal{L}_{,\Phi} [\delta\Phi] dV_0 &= \int_{\partial\Omega_0} N_I (\varepsilon J C_{IJ}^{-1} \tilde{E}_J \delta\Phi) dS_0 \\ &- \int_{\Omega_0} (\varepsilon J C_{IJ}^{-1} \tilde{E}_J - Q) \delta\Phi_{,I} dV_0 = 0 \end{aligned} \quad (58a)$$

$$\begin{aligned} \int_{\Omega_0} \mathcal{L}_{,\mathbf{A}} [\delta\mathbf{A}] dV_0 &= \int_{\partial\Omega_0} N_L (\varepsilon_{KLM} Q_M \delta A_K) dS_0 \\ &- \frac{2}{p} \int_{\partial\Omega_0} A_{R,R} N_K \delta A_K dS_0 \\ &+ \int_{\Omega_0} \varepsilon_{SPR} Q_P \frac{\partial}{\partial X_R} \delta A_S dV_0 - \int_{\Omega_0} \frac{d}{dt} \varepsilon J C_{KJ}^{-1} \tilde{E}_J \delta A_K dV_0 \\ &- \int_{\Omega_0} \sigma J C_{KI}^{-1} E_I \delta A_K dV_0 \end{aligned}$$

$$+\frac{2}{p} \int_{\Omega_0} A_{R,R} \delta A_{K,K} dV_0 = 0 \quad (58b)$$

where the condensed term is expressed as:

$$Q_M = \frac{1}{\mu J} C_{MN} B_N + \varepsilon_{MNP} \frac{\partial X_N}{\partial t} \varepsilon J C_{PQ}^{-1} \tilde{E}_Q \quad (59)$$

The weak forms in Eqs. (58a) and (58b) reduce to the strong forms in Eqs. (46a) and (46b). The scalar potential Φ and vector potentials \mathbf{A} are the solutions of Eqs. (58a) and (58b).

3.2.1 Boundary conditions in terms of the potentials

Since potential functions are chosen as primary variables in the solution of the EM field, the actual physical boundary conditions should be represented in terms of the scalar and vector potentials in the reference configuration. This is obtained by replacing the field variables with the potential expressions in the boundary term of the weak form Eq. (58a), i.e.,

$$\begin{aligned} & \int_{\partial\Omega_0} N_I \left(\varepsilon_0 J C_{IJ}^{-1} \tilde{E}_J \delta\Phi \right) dS_0 \\ &= \int_{\partial\Omega_0} N_I \left[\varepsilon_0 J C_{IJ}^{-1} (-\Phi_{,J} - \dot{A}_J \right. \\ & \quad \left. + \varepsilon_{JLK} \frac{\partial X_L}{\partial t} \varepsilon_{KMN} A_{N,M} \right) \delta\Phi \right] dS_0 \end{aligned} \quad (60)$$

where $\delta\Phi$ is the variation of Φ . For Dirichlet boundary conditions, e.g. applied voltage $V = \Phi = \Phi_0$ in electrostatic problem or for grounded boundary $\Phi = 0$, $\delta\Phi = 0$. More investigation is needed for parts of the boundary that are not governed by the Dirichlet boundary condition. For example, the boundary equation for the reference electric displacement field D_I in Eq. (35) is $N_I D_I = \rho_s$, where ρ_s is the surface charge density. This boundary condition can be implemented by substituting the value of surface charge density. Another boundary condition that can be expressed using Eq. (60) is current injection, which is governed by the reference configuration Ohm's law Eq. (38). Assuming a fixed boundary in Eq. (33) i.e. $\frac{\partial X}{\partial t} = 0$, the boundary condition reduces to:

$$\begin{aligned} & \int_{\partial\Omega_0} N_I \left[\varepsilon J C_{IJ}^{-1} (-\Phi_{,J} - \dot{A}_J) \right] \delta\Phi dS_0 \\ &= \int_{\partial\Omega_0} N_I \left[\varepsilon \frac{J_I}{\sigma} \right] \delta\Phi dS_0 \end{aligned} \quad (61)$$

This mixed form may be used to introduce the injected current along the surface normal.

The next step is to examine the boundary condition associated with the weak form in Eq. (58b). Following the same

procedure as before, the boundary terms corresponding to the Dirichlet type condition reduce to:

$$\begin{aligned} & \int_{\partial\Omega_0} N_L \left[\varepsilon_{KLM} \left(\frac{1}{\mu J} C_{MN} B_N \right. \right. \\ & \quad \left. \left. + \varepsilon_{MRP} \frac{\partial X_R}{\partial t} \varepsilon J C_{PQ}^{-1} \tilde{E}_Q \right) \delta A_K \right] dS_0 \\ & - \frac{2}{p} \int_{\partial\Omega_0} A_{R,R} N_K \delta A_K dS_0 \end{aligned} \quad (62)$$

This includes boundary condition terms from both the Maxwell's equation and the gauge condition. When values of A_I are prescribed on the boundary, both terms in Eq. (62) go to zero. This simple boundary condition is associated with the magnetic field $\mathbf{B} = \mathbf{0}$ at the boundary. From Eq. (37) it is evident that for conditions other than the Dirichlet boundary condition, Eq. (62) will hold when $N_I \times H_I$ is assigned to the boundary. This result has the physical manifestation of the surface current.

To understand the effect of the first term in Eq. (62), a fixed and undeformed boundary is assumed, thus yielding the relation:

$$\begin{aligned} & \int_{\partial\Omega_0} N_L \left[\varepsilon_{KLM} \left(\frac{1}{\mu J} C_{MN} B_N \right) \delta A_K \right] dS_0 \\ &= \int_{\partial\Omega_0} \mathbf{N} \times \left[\frac{1}{\mu J} (\nabla \times \mathbf{A}) \right] \delta \mathbf{A} dS_0 \end{aligned} \quad (63)$$

Using a vector identity this may be rewritten as:

$$\begin{aligned} & \int_{\partial\Omega_0} \mathbf{N} \times \left[\frac{1}{\mu J} (\nabla \times \mathbf{A}) \right] \delta \mathbf{A} dS_0 = \int_{\partial\Omega_0} \frac{1}{\mu J} [\nabla_A (\mathbf{N} \cdot \mathbf{A}) \\ & - (\mathbf{N} \cdot \nabla) \mathbf{A}] \delta \mathbf{A} dS_0 \end{aligned} \quad (64)$$

Here $\mathbf{N} \cdot \mathbf{A} = A^n$ is the scalar component of the vector potential \mathbf{A} normal to the surface. ∇_A is the Feynman subscript notation, which implies that the subscripted gradient operates only on \mathbf{A} . The other part is expressed as $(\mathbf{N} \cdot \nabla) \mathbf{A} = \frac{\partial \mathbf{A}}{\partial N}$, which corresponds to the flux, and hence the Neumann boundary condition in terms of \mathbf{A} . If a tangential magnetic field is imposed on the boundary, there is no normal component of A^n and the gauge condition term vanishes. If the boundary is considered as a magnetic wall, the Neumann boundary condition in terms of \mathbf{A} should be considered for a fixed and undeformed boundary.

3.3 Finite element implementation of coupled ME–EM problem

Numerical implementation of the weak forms and boundary conditions is conducted for the coupled problem using

a staggered approach, where the dynamic displacement field is solved first followed by the electromagnetic problem. The semidiscretization method involving separation of variables is used to represent the variables as discrete functions of space, yet continuous functions of time. For 8-noded brick elements, independent variables (displacements, scalar and vector potentials) of the coupled problem in each element e are interpolated as:

$$\begin{aligned} \mathbf{u}^e(\mathbf{X}, t) &\approx \sum_{\alpha=1}^8 \mathbf{u}_{\alpha}^e(t) N_{\alpha}^e(\mathbf{X}), \\ \Phi^e(\mathbf{X}, t) &\approx \sum_{\alpha=1}^8 \Phi_{\alpha}^e(t) N_{\alpha}^e(\mathbf{X}), \\ \mathbf{A}^e(\mathbf{X}, t) &\approx \sum_{\alpha=1}^8 \mathbf{A}_{\alpha}^e(t) N_{\alpha}^e(\mathbf{X}) \end{aligned} \tag{65}$$

where $N(\mathbf{X})$ are trilinear isoparametric shape functions of the brick element [27]. Note that both the mechanical and electromagnetic field variables adopt the same finite element mesh. The implicit time integration Newmark-beta method, which assumes constant average acceleration in each time step [28], is implemented for integrating the dynamic problems. Both the initial displacement and velocity are set to be zero, i.e. $\mathbf{u}(\mathbf{X}, 0) = \mathbf{0}$, $\dot{\mathbf{u}}(\mathbf{X}, 0) = \mathbf{0}$. The backward Euler method is implemented for integrating the EM fields as:

$$\begin{aligned} \dot{\Phi}^e(\mathbf{X}, t_n) &\approx \frac{\Phi_{\alpha}^e(t_n) - \Phi_{\alpha}^e(t_{n-1})}{\Delta t} N_{\alpha}^e(\mathbf{X}) \\ \dot{\mathbf{A}}^e(\mathbf{X}, t_n) &\approx \frac{\mathbf{A}_{\alpha}^e(t_n) - \mathbf{A}_{\alpha}^e(t_{n-1})}{\Delta t} N_{\alpha}^e(\mathbf{X}) \end{aligned} \tag{66}$$

where Δt is time step that is determined from the higher frequency response in the coupled problem. For the electromagnetic field, $\Phi(\mathbf{X}, 0)$ is set to be zero throughout domain except for certain boundary conditions. The vector potential \mathbf{A} and its rate $\dot{\mathbf{A}}$ are obtained from the solution of the problem with $\Phi(\mathbf{X}, 0) = 0$.

For efficient computing of the large degrees of freedom (DOF) coupled ME–EM model, the finite element code is parallelized using available libraries. The ParMETIS [29] library is utilized to decompose the computational domain and distribute to multiple processors. Subsequently, the Portable, Extensible Toolkit for Scientific Computation or PETSc [30] library, which is a Message Passing Interface (MPI) based library, is employed to accomplish parallelization of the code. Both the ME and EM codes are developed using PETSc to guarantee the same structure. A linear solver, SuperLU [31] is used to solve the matrix equations. Details of the solution methodology for the coupled problem are shown in the flowchart of Fig.1.

4 Numerical examples simulated with the coupled dynamic electromagnetic (ME–EM) code

Numerical examples, simulated using one-way coupled dynamic, electromagnetic (ME–EM) code, are divided into two categories. The first category corresponds to validation examples, where the results of simulation with the code are compared with existing analytical solutions or results from commercial software like COMSOL [32] and ANSYS [33]. These packages generally have limited capacity with respect to solving coupled, dynamic electromagnetic problems. Correspondingly, selected features of the ME–EM code are tested against these codes. The comparisons are respectively made for (a) an electro-static problem, (b) a magneto-static problem, (c) a transient magnetic problem, and (d) a transient electromagnetic problem, all without mechanical excitation. Subsequent to the validation tests, the code is used to simulate two example, coupled ME–EM problems. The first example is for a steady-state electromagnetic field in a dynamically loaded structure. The second example solves a transient electromagnetic field problem in a structure undergoing finite deformation under dynamic condition. These examples demonstrate the effectiveness of the coupled mechanical-electromagnetic code and model.

4.1 Validation examples

4.1.1 Electrostatic problem for a micro-strip

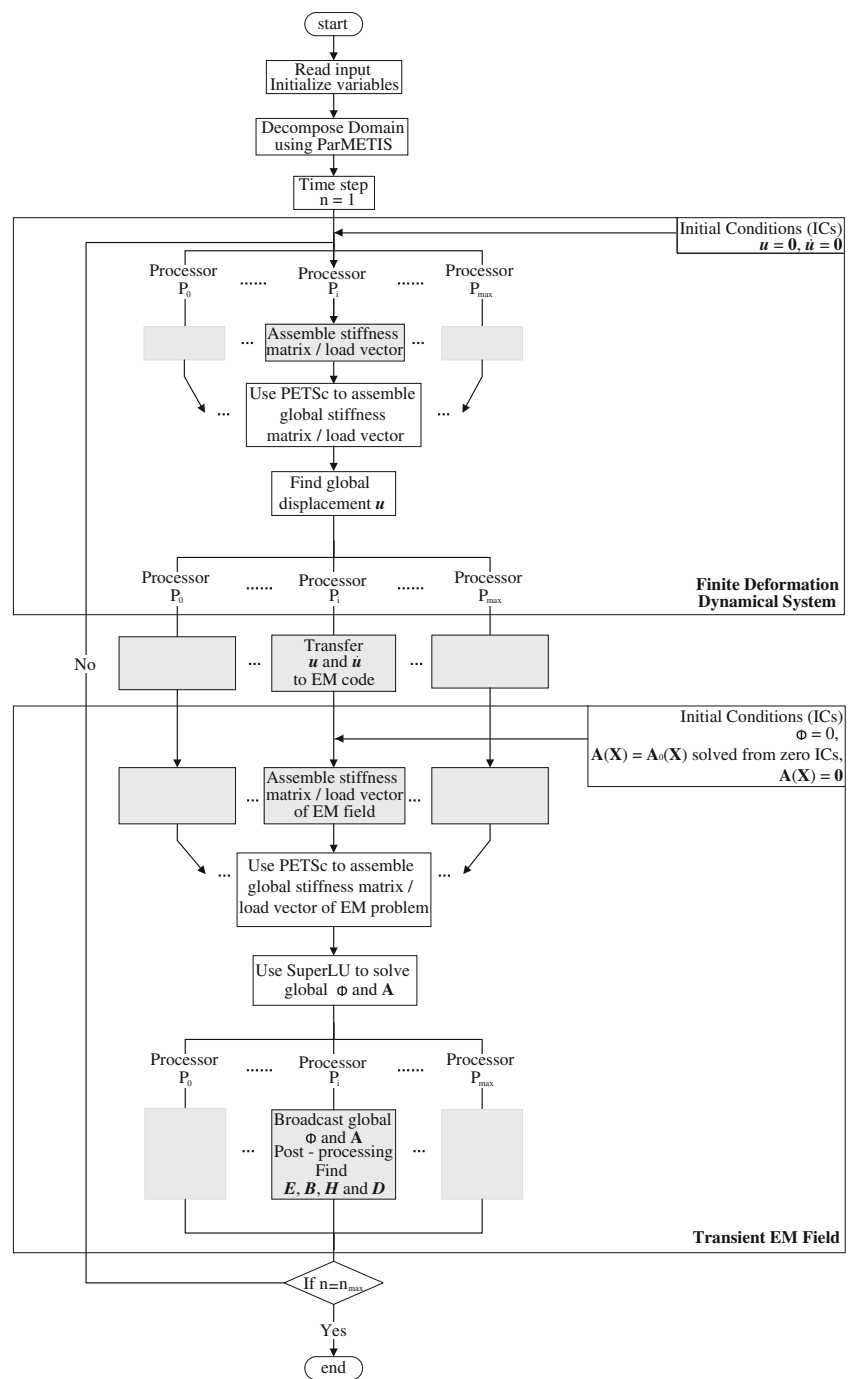
Electrostatic problems of a shielded micro-strip have been discussed in [24] and also in COMSOL AC/DC module tutorial model [32] primarily in 2D. The corresponding 3D model, solved using the ME–EM code, is illustrated in Fig. 2a. A homogenous Neumann boundary condition is applied on the lateral boundary in z direction, which keeps any field from transmitting across the interface. This boundary condition also helps in reducing the model dimensions due to half-symmetry. In the ME–EM code, the mechanical response is frozen for this problem and hence the current and reference configurations are identical. Only the scalar potential φ is relevant for this electrostatic problem. In this setting, the governing equations Eq. (43a) and Eq. (43b) are reduced to

$$\nabla^2 \varphi = -q_e \tag{67}$$

Figure 2 shows the dimensions of the $10 \times 10.5 \times 6 \text{ mm}^3$ computational domain with boundary conditions. For the inner conductor, the potential is $\varphi = 1 \text{ V}$, while the shielding conductor has a scalar potential value of $\varphi = 0 \text{ V}$ assigned to the outer boundary.

Results of simulation with the ME–EM code containing 158976 8-noded brick elements are shown in Fig. 3a. The permittivity of the dielectric is chosen to be $\epsilon = 1.0 \text{ F/m}$

Fig. 1 Flow chart of the coupled mechanical and EM field problem



simplicity in post-processing. The contour plot is for the distribution of the electric potential φ , while the arrows indicate the electric field. The length and direction of the arrow correspond to the magnitude and direction of the electric field at each nodal point. Comparison of the results of the ME–EM code with two different 3D mesh densities, and the COMSOL code with a 2D mesh are shown in Fig. 3b. The results demonstrate good agreement in the distribution of the scalar potential, even with a relatively coarse ME–EM mesh. The electric potential decays from 1 V at the inner boundary to 0 at the outer boundary. To study convergence of the ME–

EM model and code, seven additional mesh densities are simulated. The finest mesh shown in Fig. 2 contains 159876 brick elements, whose solution is referred to as the reference solution. The error with respect to the reference solution is evaluated using the L_2 norm of φ in the domain, defined as:

$$\|e\|_{L_2} = \frac{\left[\int_{\Omega} (\varphi - \hat{\varphi})^T (\varphi - \hat{\varphi}) d\Omega \right]^{\frac{1}{2}}}{\left(\int_{\Omega} \varphi^T \varphi d\Omega \right)^{\frac{1}{2}}}. \quad (68)$$

where φ is the reference electric potential solution in the finest mesh model. The corresponding error plot is shown

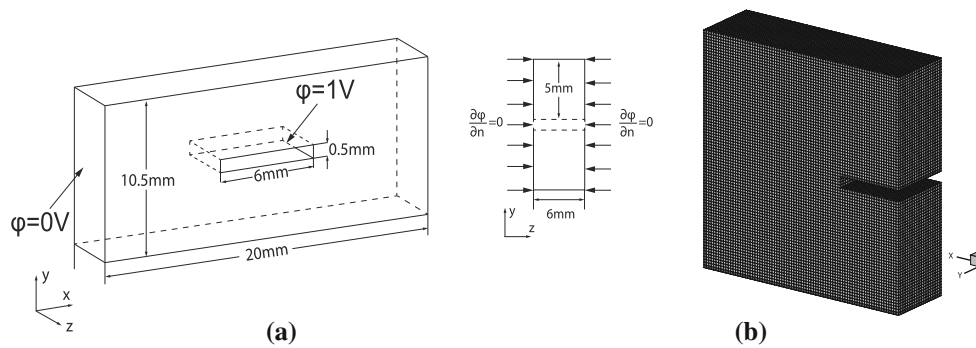


Fig. 2 Microstrip model and boundary conditions. **a** 3D model with homogenous Neumann boundary condition on lateral boundaries in the z direction. **b** Mesh of ME-EM FE code containing 158976 brick elements for the half-symmetry model

Fig. 3 **a** Scalar potential and electric field distribution in the 3D microstrip model using the ME-EM code. **b** comparison of scalar potential distribution along x -axis generated by the ME-EM code and COMSOL

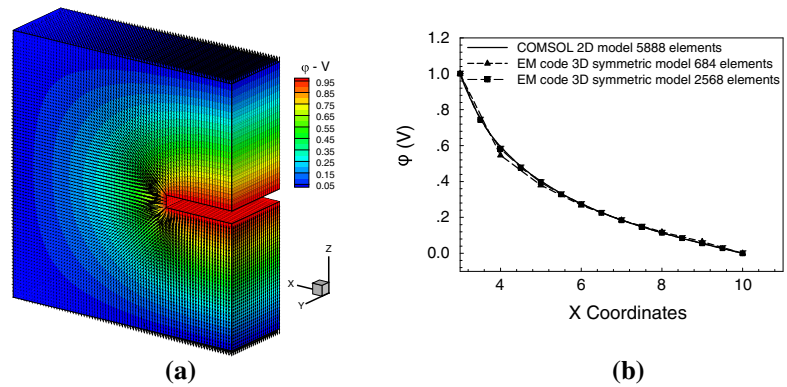
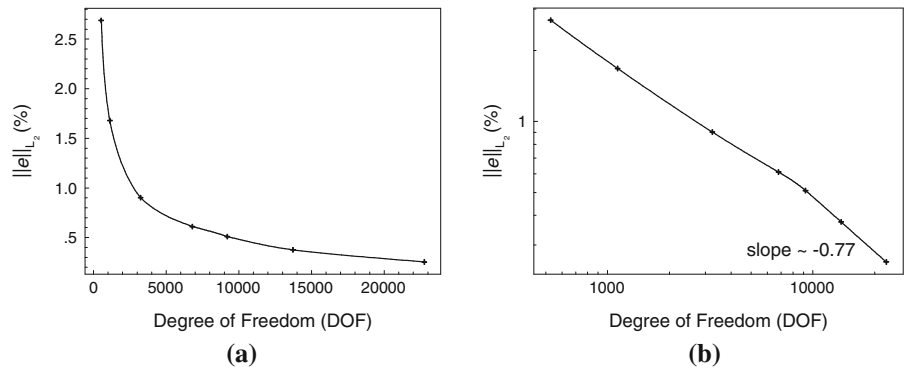


Fig. 4 **a** Plot of the error $\|e\|_{L_2}$ with increasing DOF. **b** Convergence rate of results with the ME-EM code



in Fig. 4a, exhibiting convergence with increasing degrees of freedom (DOF). The rate of convergence is shown in the log-log plot ($\log \|e\|_{L_2} \approx \log k - \beta \log N$ where N is the DOF) of Fig. 4b, with a slope of $\beta = 0.77$.

4.1.2 Magnetostatic problem with current injection

This example simulates the response of a rectangular conductor, shown in Fig. 5, with an injected steady-state direct current, and compares it with results using the COMSOL code. For steady-state electromagnetic fields or in cases where the transients are not significant enough to produce induction terms, the electric and magnetic fields are decoupled and can be solved independently. When the current inside the conduc-

tor reaches steady-state, the magnetic field in this magneto-static problem is expressed as:

$$\nabla^2 \mathbf{a} = -\mu_0 \mathbf{j}, \tag{69}$$

which is reduced from Eq. (43b) by neglecting the time-dependent contributions of the scalar and vector potentials. Additionally, the gauge condition reduces to $\nabla \cdot \mathbf{a} = 0$. Instead of assigning the point-wise current density inside conductor, this problem is solved by using the ME-EM code, for which the governing equations are obtained by substituting the gauge condition and Ohm's law $\mathbf{j} = \sigma \mathbf{e} = \sigma(-\nabla\phi - \frac{\partial \mathbf{a}}{\partial t})$ in Eqs. (43a) and (43b) in the absence of deformation. The corresponding equations are:

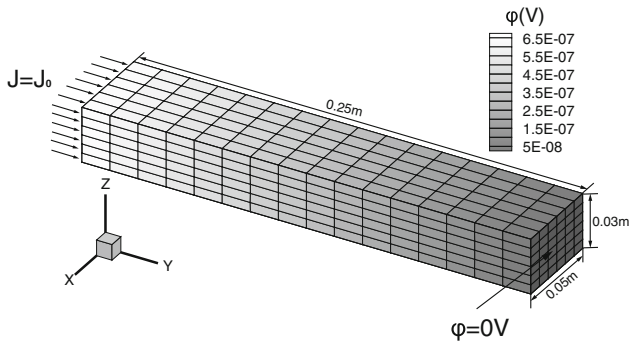


Fig. 5 FE model and mesh of the rectangular conductor showing current injection as well as electric potential distribution

$$\nabla^2 \varphi = -q_e \tag{70a}$$

$$\left(\nabla^2 a_i - \mu \varepsilon \frac{\partial^2 a_i}{\partial t^2} \right) - \left(\mu \varepsilon \frac{\partial \varphi}{\partial t} \right)_{,i} = \mu \sigma \left(\varphi_{,i} + \frac{\partial a_i}{\partial t} \right) \tag{70b}$$

The current density in the conductor, in the right hand side of Eq. (69), is imposed by the mixed boundary condition given in Eq. (61), which assigns direct current injected from one end. The conductor is grounded at the other end that is manifested by setting the scalar potential to $\varphi = 0$. The lateral sides are kept from any current flow by imposing a Dirichlet boundary condition for the vector potential, i.e. $\mathbf{a} = \mathbf{0}$. After the solution reaches the steady-state, the time dependent terms in Eq. (70a) and Eq. (70b) drop off. Both scalar potential and vector potential are obtained as solutions. The results of ME–EM code are compared with those of COMSOL simulation in Fig. 6, which shows φ at the middle point of the surface where current is injected. The conducting material is considered to be aluminum, for which the permittivity is $\varepsilon = 7.0832 \times 10^{-11}$ F/m, the permeability is $\mu = 1.2567 \times 10^{-6}$ H/m and the conductivity is $\sigma = 37.8 \times 10^6$ S/m. Since the ME–EM code has transient effects, results of the magnetostatic problem are achieved in the steady-state limit. Figure 6 shows that the results approach the steady-state value faster with smaller time steps. This convergence trend is an indicator of stability of the ME–EM code.

4.1.3 Transient magnetic field problem

This example, discussed as case VM167 in the ANSYS verification manual [33], deals with the development of a transient magnetic field in a static semi-infinite conductor. At start, the vector potential \mathbf{a} in the conductor is zero, while at $t = 0^+$ a pulse in \mathbf{a} is imposed on the boundary that generates a transient magnetic field through the conductor. An eddy current field is rendered in the governing equations by removing the time-dependent electric displacement field in Eq. (8d). With the constitutive relation in Eq. (10) and zero scalar potential,

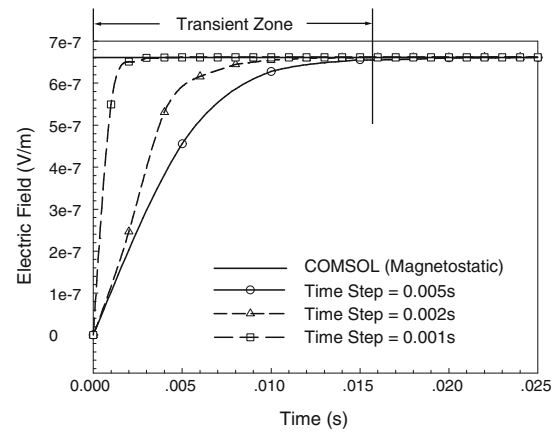


Fig. 6 Convergence of electric field with different time steps for magnetostatic simulations by the ME–EM code

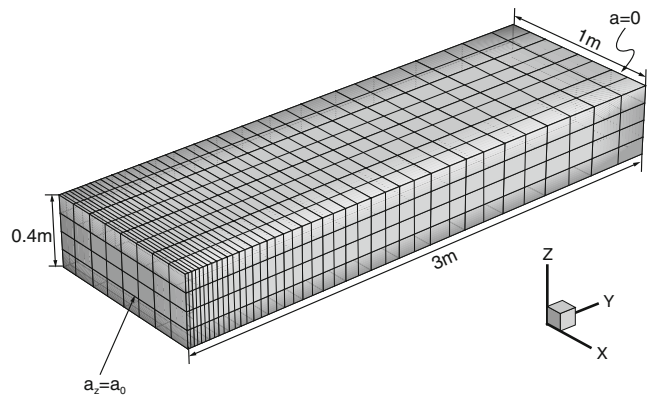


Fig. 7 Model of transient magnetic field problem in ME–EM code, the gradient mesh in y direction is kept same as that of in ANSYS

the governing equation after applying the gauge condition $\nabla \cdot \mathbf{a} = 0$, reduces to:

$$\nabla^2 \mathbf{a} - \mu \sigma \frac{\partial \mathbf{a}}{\partial t} = 0, \tag{71}$$

In ANSYS [33], the semi-infinite conductor is modeled in 2D as a thin wire with a graded mesh to better capture the signal near the boundary where the pulse vector is applied. On the other end, a homogenous Dirichlet boundary condition $\mathbf{a} = \mathbf{A} = 0$ is applied. The corresponding computational domain with graded mesh and boundary conditions for the 3D ME–EM model are depicted in Fig. 7. The material permeability is $\mu = 1.2567 \times 10^{-6}$ H/m and the conductivity is $\sigma = 2.5 \times 10^6$ S/m. The transient vector potential and induced eddy current are monitored for the domain and reported for a point near the boundary where the pulse is imposed and transient results are sensitive. A minimum time step of $\Delta t = 0.0002$ s is used in the simulations. Comparison of results by the ME–EM code and ANSYS are shown in Fig. 8a. As observed, the ME–EM code is able to capture and reproduce the transients simulated in ANSYS. An time-dependent error

Fig. 8 Transient magnetic field simulation results: **a** comparison of vector potential in the z direction between results generated by the ME–EM code and ANSYS; **b** local error with evolving time

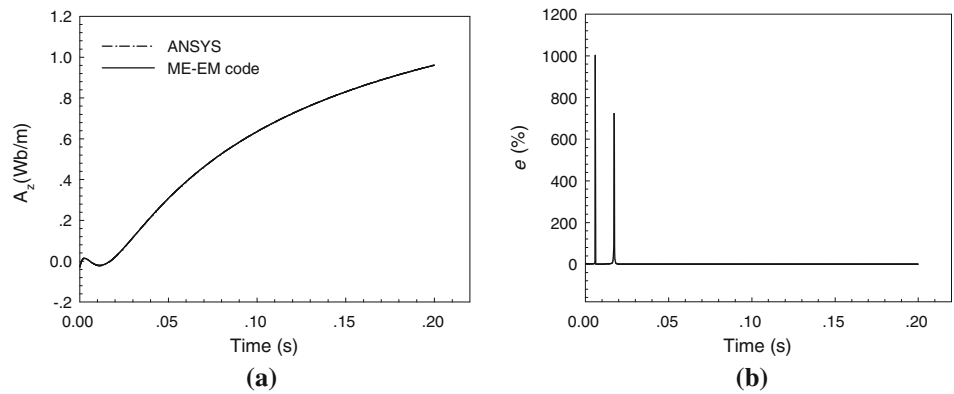
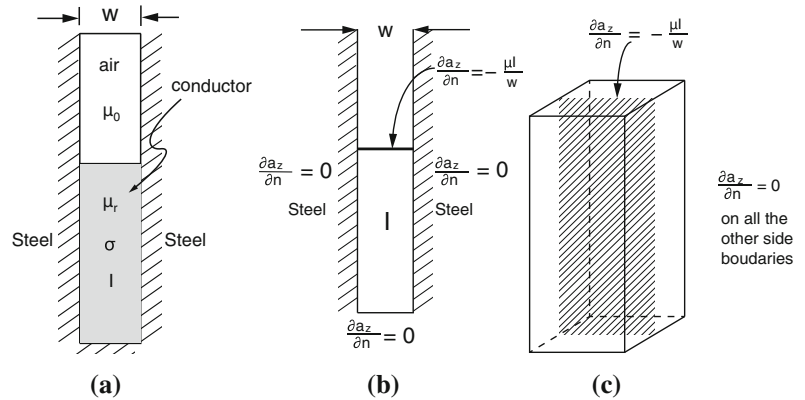


Fig. 9 **a** A slot embedded conductor simulated in the transient electromagnetic model. **b** Equivalent boundary conditions on the conductor domain boundaries, thus avoiding free-space. **c** 3D FE model of the conductor implemented in the ME–EM code



measure between the ME–EM and ANSYS results is defined as $e(t) = \frac{(A_z^{ANSYS}(t) - A_z^{EM}(t))^2}{(A_z^{ANSYS}(t))^2} \times 100\%$ and plotted in Fig. 8b. While initial transient effects give rise to a few spikes in error, it quickly subsides to zero with time.

4.1.4 Transient electromagnetic field problem

This final validation example explores a coupled, transient electric and magnetic field problem using the ME–EM code by simulating the transient response due to alternating current (AC) in a slot embedded conductor. The problem is introduced as a case study VM186 in the ANSYS verification manual [33], as well as in [34] for studying skin effect. The geometric model contains three parts, viz. air, conductor and steel as shown in Fig. 9a. The conductor carries a current I in the axial direction, perpendicular to its cross section. The permeability of the conductor is $\mu = 1.0$ H/m while its conductivity is $\sigma = 1.0$ S/m. In the governing equations (72), the total measurable current is comprised of two parts, viz. (a) a source current I_s determined by the scalar potential and (b) an eddy current I_e which is induced by the time derivative of the vector potential. Since the scalar and vector potentials are independent variables to be solved from Eq. (72), I_s and I_e are a-priori unknown.

$$\nabla^2 \varphi = -q_e \tag{72a}$$

$$\nabla^2 a_i - \left(\mu \varepsilon \frac{\partial \varphi}{\partial t} \right)_{,i} = \mu \left(\underbrace{\varphi}_{I_s}, i + \sigma \underbrace{\frac{\partial a_i}{\partial t}}_{I_e} \right) \tag{72b}$$

The values of permeability for steel and the conductor material are significantly different, which makes it difficult to transmit magnetic flux across the interface. This assumption restricts the magnetic field to be within the conducting slot and hence only the conductor is simulated. A homogenous Neumann boundary condition, in terms of the gradient of the vector potential, is imposed on the interface between conductor and steel to generate a magnetic wall as shown in Fig. 9b. The effect of EM fields in the free space or air is incorporated through an equivalent boundary condition as given in [35]. The computational domain is reduced to the conductor only by adding a Neumann boundary condition on the interface between conductor and air as:

$$\frac{\partial a_z}{\partial n} = -\frac{\mu I}{w} \tag{73}$$

Here w is the width of the cross-section as shown in Fig. 9b. The 3D computational model with boundary conditions are depicted in Fig. 9b, c.

Fig. 10 Comparison of the results of transient electromagnetic field simulations by the ME–EM code and ANSYS: **a** total and eddy current results simulation; **b** rate of convergence with decreasing time steps

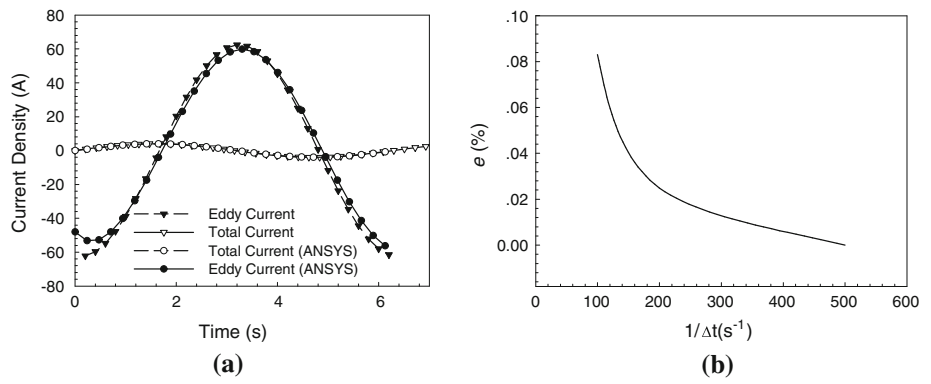
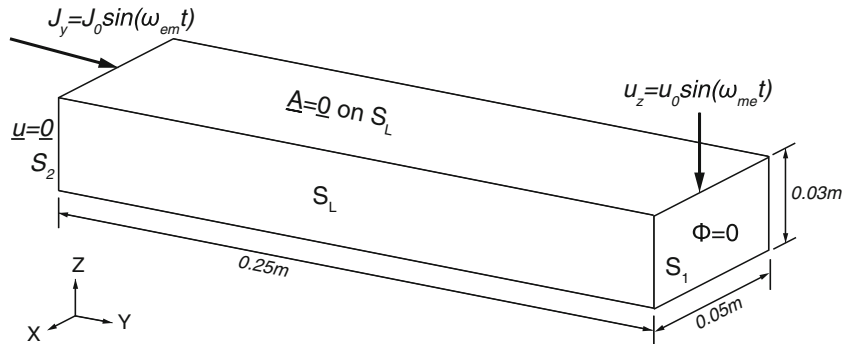


Fig. 11 Schematic model of a vibrating conductor with injected current. The mechanical loading is in z -direction, and the current injects through y -direction



Results of simulations, in terms of the total current and the eddy current, by the ME–EM code and ANSYS are compared in Fig. 10a. While the results are generally in good agreement, a small difference in the early time steps arises from the initial conditions. To comprehend convergence of the ME–EM results with decreasing time-steps, simulations are conducted with different time steps Δt and an error measure e is defined as:

$$e = \left\| \frac{I^{ME-AM}(\Delta t) - I^{ANSYS}}{I^{ANSYS}} \right\| \quad (74)$$

The error is plotted as a function of the inverse of the time step, i.e. $\frac{1}{\Delta t}$. It reduces rapidly with decreasing time-steps as shown in Fig. 10b.

4.2 Coupled mechanical and electromagnetic field simulations

Subsequent to validation of the electromagnetic part of the model and code, this section examines its abilities in predicting the evolution of coupled, dynamic and transient electromagnetic fields in multi-physics problems. Two examples are specifically considered in this section. The first examines the effect of dynamic deformation on steady-state electromagnetic fields in a conductor, while the second example explores its effect on transient electromagnetic field variables. For both examples, the conducting substrate is a rectangular plate as shown in Fig. 11. The logarithmic stretch

model is employed. The mechanical properties in Eq. (6) are given in terms of the Lamé constants as $\lambda = 40.4$ GPa and $\mu = 26.9$ GPa respectively, and the electromagnetic properties in Eqs. (10) are: $\epsilon = 7.0832 \times 10^{-11}$ F/m, $\mu = 1.2567 \times 10^{-6}$ H/m and $\sigma = 37.8 \times 10^6$ S/m. The deforming conductor is fixed at one end, i.e. $\mathbf{u} = \mathbf{0}$ on S_2 . The other end S_1 is subjected to a z -direction sinusoidal excitation $u_z(t) = u_0 \sin(\omega_{me} t)$. For the EM problem, the top, bottom and side surfaces, designated as S_L , are assigned homogeneous Dirichlet boundary conditions for the vector potential i.e. $\mathbf{A} = \mathbf{0}$ in the reference configuration. A current $J_y(t) = J_0 \sin(\omega_{em} t)$ is injected into the fixed end S_2 of the conductor. S_1 is grounded by setting scalar potential $\Phi = 0$ in the reference configuration. Values of the displacement parameters (u_0, ω_{me}) and current parameters (J_0, ω_{em}) are varied for the different examples in this section.

4.2.1 Effect of dynamically deforming substrate on steady-state electromagnetic field

This example represents a coupled multiphysics problem, in which the steady-state electromagnetic field is unilaterally affected by deformation fields in a dynamically loaded conducting substrate. The EM field is affected by various characteristics of the mechanical field, viz. (i) loading direction, (ii) displacement amplitude, (iii) velocity amplitude and (iv) loading frequency. The effect of direction is first examined

with excitations perpendicular and parallel to the EM source, followed by the other characteristics.

In the first simulation, the face S_1 is subjected to a z -direction sinusoidal excitation $u_z(t) = u_0 \sin(\omega_{me}t)$, where $u_0 = 0.2$ m and $\omega_{me} = 100$ Hz. Here the mechanical excitation direction is perpendicular to the EM source as shown in Fig. 11. A constant direct current $J_0 = 200$ A, $\omega_{em} = 0$ is injected into the fixed end S_2 . For each time step, the EM field variables \mathbf{E} , \mathbf{B} , \mathbf{D} and \mathbf{H} in the reference configuration are obtained by Eqs. (45a), (45b), (35) and (37) respectively, following which the current configuration field variables \mathbf{e} , \mathbf{b} , \mathbf{d} and \mathbf{h} are calculated using transformations in Eqs. (34), (32), (18a) and (36). For a fixed conductor, the injected current will induce a steady-state y -direction electric field e_y . However with sinusoidal excitation, the electric field e_y at a point ($x = 0.025$ m, $y = 0.125$ m, $z = 0.015$ m) evolves following the orthogonal, time-harmonic velocity v_z as shown in Fig. 12a. The frequency of e_y is double the frequency of v_z , which is perpendicular to e_y arising from the cross product of velocity and EM fields in Eqs. (58a) and (58a). To comprehend the effect of load direction on EM frequency, the mechanical excitation is applied in the y direction instead of the z direction, i.e. $u_y(t) = u_0 \sin(\omega_{me}t)$ in Fig. 11 with $u_0 = 0.04$ m and $\omega_{me} = 100$ Hz. Here the mechanical and EM loadings are in the same direction. The cross product vanishes, yielding the same frequency for e_y and v_z as shown in the plot of Fig. 12b. Thus, while the amplitude of oscillation of e_y is not significantly affected by the direction of mechanical fields, it has a more profound effect on the EM frequency.

Next, the influence of the amplitude and frequency of mechanical excitation $u_z(t) = u_0 \sin(\omega_{me}t)$ in Fig. 11, on the EM field is considered. Three specific cases are studied, viz. (i) $u_0 = 0.2$ m, $\omega_{me} = 100$ Hz, (ii) $u_0 = 0.2$ m, $\omega_{me} = 200$ Hz and (iii) $u_0 = 0.1$ m, $\omega_{me} = 200$ Hz. The effect of the excitation frequency and amplitude of velocity compared for the results from (i) and (ii). Fig. 13a plots e_y for the corresponding two frequencies. Both the amplitude and frequency of the electric field e_y are affected by changes in ω_{me} . The frequency ω_{em} of e_y nearly doubles, consistent with the change in ω_{me} . The amplitude of e_y also changes, even though the displacement amplitude is unchanged. This is due to the increased (nearly doubled) amplitude of velocity with doubled ω_{me} . The maximum amplitude of e_y increases from 1.023×10^{-5} V/m to 1.821×10^{-5} V/m for frequency change from $\omega_{me} = 100$ Hz to $\omega_{me} = 200$ Hz. The corresponding change in the minimum amplitude is small from 3.437×10^{-6} V/m to 2.928×10^{-6} V/m. This infers that the velocity field v_z affects the amplitude of e_y in a nonlinear fashion. The excitation displacement amplitude for case (iii) is half of the other two, while its velocity amplitude is the same as case (ii). Results of cases (i) and (iii) reveal the influence of magnitude of the displacement field on the EM

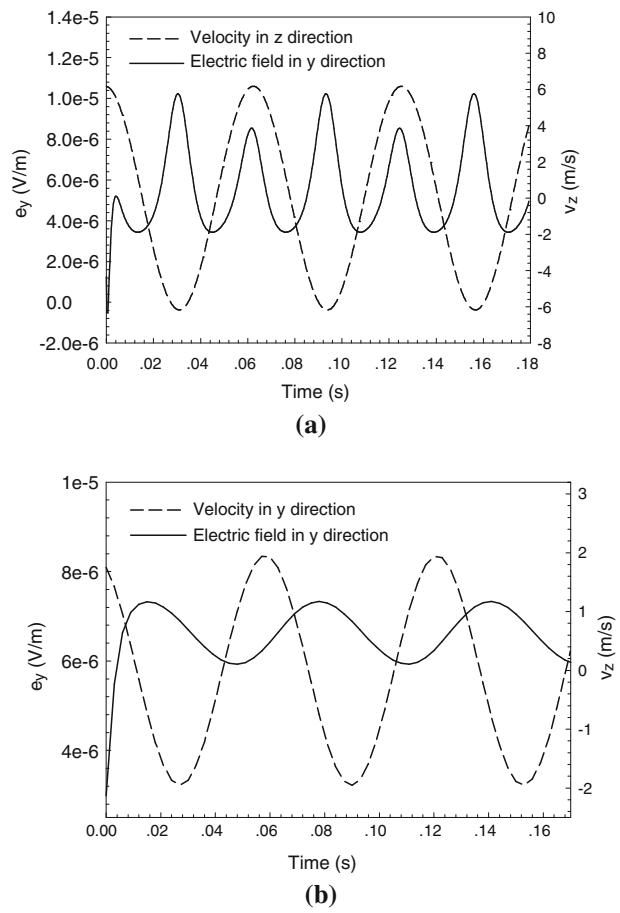


Fig. 12 Plot of the velocity velocity and electric field components as functions of time: **a** v_z and e_y ; **b** v_y and e_y

field. Figure 13b shows that the maximum amplitude of e_y 1.012×10^{-5} V/m for (iii) is almost the same as the amplitude 1.023×10^{-5} V/m for (i). However, the minimum amplitude increases significantly by reducing u_0 from 3.437×10^{-6} V/m for (i) to 5.137×10^{-6} V/m for (iii). From Figs. 13a, b, it may be concluded that the magnitude of velocity has a significant effect on the peak value of e_y , while the displacement affects the lowest values. Also the mechanical loading frequency directly determines the frequency of the EM field.

A few observations may be made from this simple example as summarized below:

- For dynamic loads parallel to a steady-state EM source, the EM field will evolve with a frequency that is similar to that of the loading. For loads orthogonal to the EM source, the EM frequency can be significantly higher due to the coupling.
- The amplitude of the applied displacement affects the lower values of the oscillatory EM field, while the amplitude of the velocity field affects the peak EM values.
- The frequency of the mechanical excitation affects the frequency of the EM field to an extent that depends on

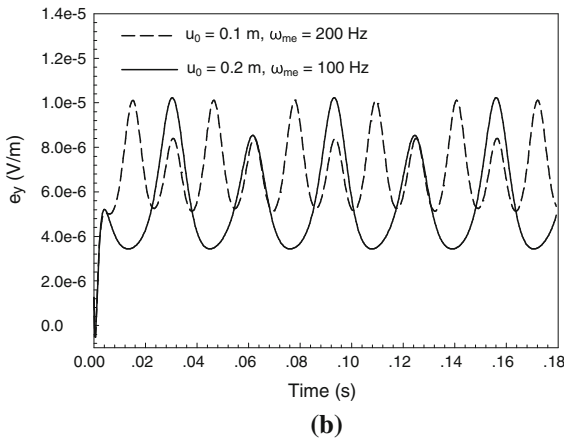
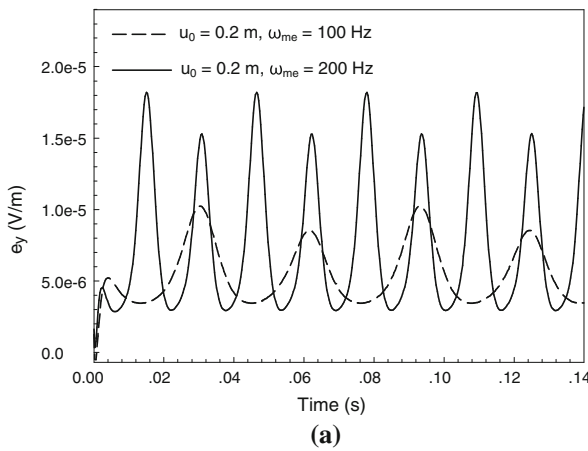


Fig. 13 Comparison of e_y for: **a** different mechanical frequencies $\omega_{me} = 100$ Hz and $\omega_{me} = 200$ Hz with $u_0 = 0.2$ m; **b** different mechanical amplitudes and frequencies $u_0 = 0.2$ m, $\omega_{me} = 100$ Hz and $u_0 = 0.1$ m, $\omega_{me} = 200$ Hz

the loading direction. The importance of coupling the two fields in a multi-physics analysis is realized through this example.

4.2.2 Effect of dynamically deforming substrate on transient electromagnetic field

This example extends the study in the previous section to a time-dependent electromagnetic field caused by an alternating current in an dynamically vibrating rectangular conductor. The current injected at the fixed end S_2 in Fig. 11 is $J_y(t) = J_0 \sin(\omega_{em}t)$, where $J_0 = 200$ A and $\omega_{em} = 500$ Hz. The effect of the AC current frequency ω_{em} , as well as the applied displacement and velocity amplitudes (u_0, v_0) on the EM field are investigated. For the examples considered, the z -direction displacement excitation has the parameters $u_0 = 0.2$ m, $\omega_{me} = 100$ Hz. Thus $\frac{\omega_{em}}{\omega_{me}} = \frac{T_{me}}{T_{em}} = 5$, where T_{me} and T_{em} are the velocity and current time-periods respectively. Figure 14 is a plot of the oscillating electric field component e_y at the centroid of the conductor. Clearly

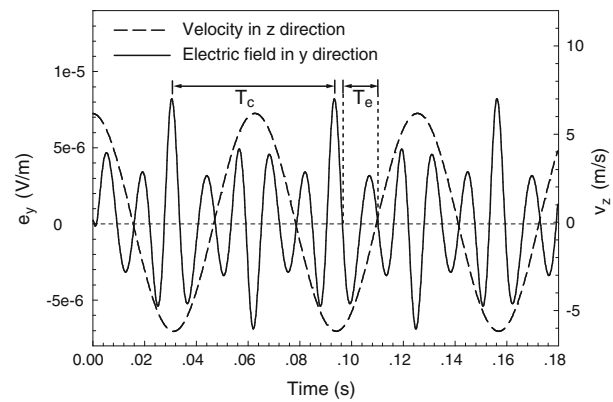


Fig. 14 Plot of e_y and v_y with time for current and mechanical frequencies $\omega_{em} = 500$ Hz, $\omega_{me} = 100$ Hz

the frequency is affected by that of both the current and mechanical excitations. The oscillations exhibit two types of response periods, viz. (i) one characterized by the shorter period T_e in Fig. 14 that follows the high frequency pattern of the imposed electric current, and (ii) a longer period T_c corresponding to the distance between two identical maximum peaks, which follows the frequency of the mechanical excitations. To study this behavior further, simulations are conducted with $\omega_{me} = 200$ Hz and $\omega_{me} = 300$ Hz respectively. The corresponding results are shown in Figs. 15a, b. It is generally observed that the longer period T_c scales with the ratio $\frac{\omega_{em}}{\omega_{me}}$, in proportion to electric current period T_{em} .

Finally, to study the effects of displacement and velocity amplitude on EM fields, three simulations with the following conditions are conducted: (i) $u_0 = 0.2$ m, $\omega_{me} = 100$ Hz, $\omega_{em} = 500$ Hz, (ii) $u_0 = 0.2$ m, $\omega_{me} = 200$ Hz, $\omega_{em} = 500$ Hz, and (iii) $u_0 = 0.1$ m, $\omega_{me} = 200$ Hz, $\omega_{em} = 500$ Hz. Figure 16a compares the result of e_y for (i) and (ii) with doubled velocity, while the comparison for the same velocity in (i) and (iii) is shown in Fig. 16b. The overall maximum peaks increase with time for both figures. However the minimum value of the signal decreases with increasing velocity thus widening the gap between the maximum and minimum values. While an increase in displacement amplitude leads to larger peak values of e_y , it reduces the minimum value thus shifting both the minimum and maximum EM amplitudes upwards. In conclusion, the resulting EM signals in the coupled system have a complicated dependence on the mechanical and EM fields that require a robust analysis capability.

5 Conclusion

This paper develops a finite element model for multi-physics analysis, coupling transient electromagnetic and dynamic mechanical fields in the time-domain. The model frame-

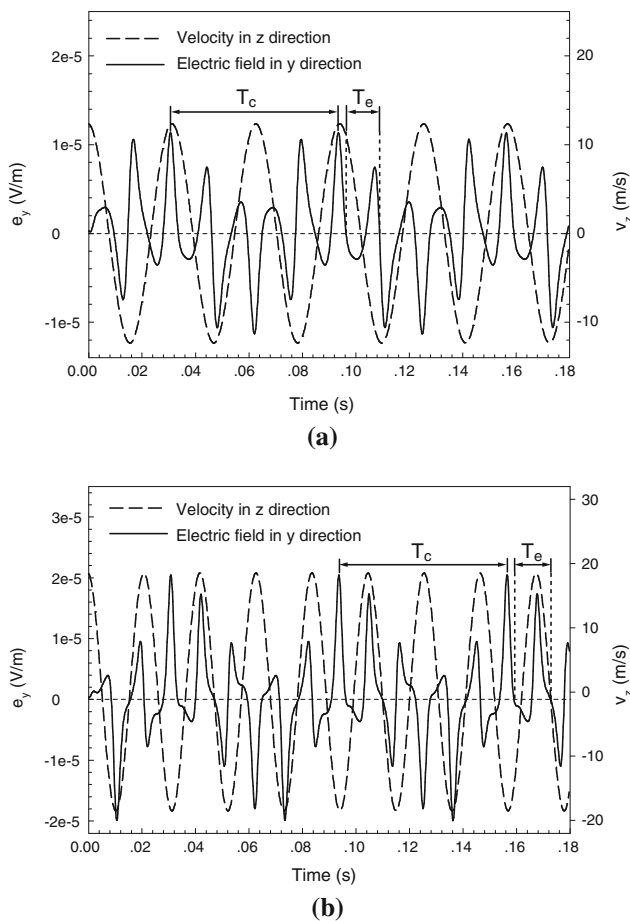


Fig. 15 Plot of e_y and v_y with time for different ratios of T_{em} and T_{me} with: **a** $\omega_{me} = 200$ Hz, $\omega_{em} = 500$ Hz and **b** $\omega_{me} = 300$ Hz, $\omega_{em} = 500$ Hz

work is able to predict the evolution of electrical and magnetic fields and their fluxes in a vibrating media undergoing finite deformation. To account for finite deformation and its effects on the electromagnetic fields, a Lagrangian description is invoked to develop the finite element formulation. In this formulation, the coupling scheme maps Maxwell’s equations from spatial to material coordinates in the reference configuration. Weak forms of the coupled transient EM and dynamic ME equations are generated in the reference configuration. For efficient solution with reduced degrees of freedom, a scalar potential and vector potential are chosen as independent solution variables in lieu of electromagnetic field variables. The introduction of the potential function can result in non-uniqueness of the electromagnetic solution, which is overcome by introducing a Coulomb gauge condition. The resulting finite element ME–EM code with large degrees of freedom is parallelized using the ParMETIS library for domain decomposition and the MPI-based PETSc library for solving.

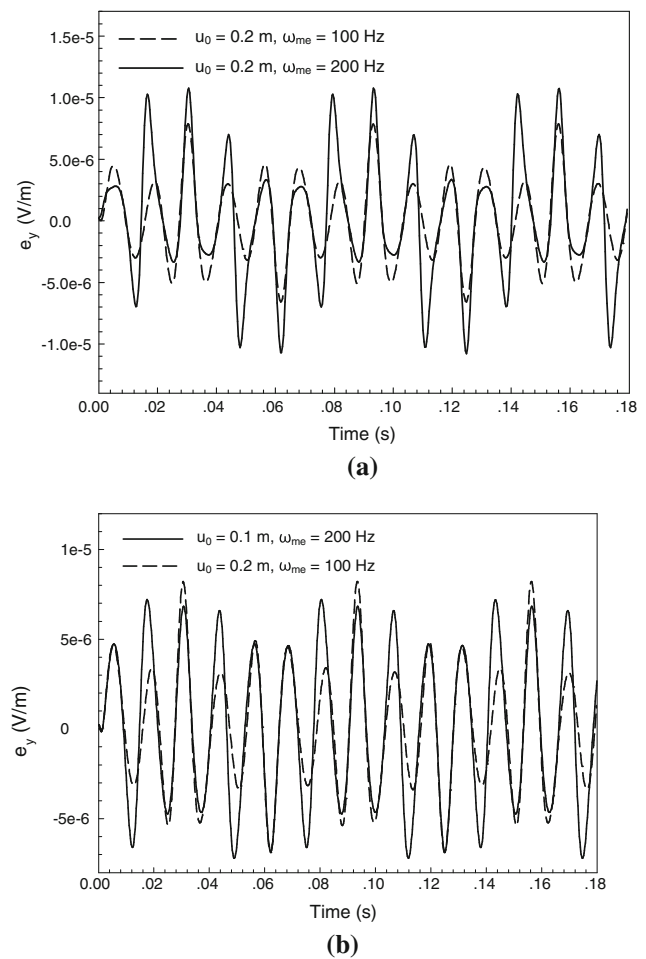


Fig. 16 Comparison of e_y for **a** varying mechanical frequency and velocity amplitude $u_0 = 0.2$ m, $\omega_{me} = 100$ Hz, $\omega_{em} = 500$ Hz and $u_0 = 0.2$ m, $\omega_{me} = 200$ Hz, $\omega_{em} = 500$ Hz; and **b** varying displacement amplitude e_y in $u_0 = 0.2$ m, $\omega_{me} = 100$ Hz, $\omega_{em} = 500$ Hz and $u_0 = 0.1$ m, $\omega_{me} = 200$ Hz, $\omega_{em} = 500$ Hz

Two categories of numerical examples are solved using the ME–EM model and code. First the electromagnetic part of the code is validated by comparing with results from commercial software like COMSOL and ANSYS for electrostatic, magneto-static, transient magnetic, and transient electromagnetic problems, without mechanical excitation. Convergence studies are made to examine the stability and accuracy of the model with satisfactory results. Subsequent to the validation tests, the ME–EM code is used to simulate two coupled ME–EM problems. The first example examines the effect of dynamic harmonic excitation of the substrate on a steady-state electromagnetic field. The effects of mechanical load frequency, amplitudes and direction on EM fields are investigated. In the second example, effects are explored for an additional transient electrical current on the boundary of the dynamically deforming conductor. Characteristics of the coupled solutions clearly demonstrate

the complexity brought about by coupling the two physical phenomena.

Acknowledgments The authors gratefully acknowledge the support of this work by the *Mechanics of Multifunctional Materials & Microsystems Program* of the Air Force Office of Scientific Research through a MURI Grant on Bio-inspired Sensory Network to Stanford University. The Program Director for this Grant is Dr. B. L. “(Les)” Lee. The specific work was done under a subcontract to Johns Hopkins University under award ID 2770925044895D.

References

1. Le Chevalier F, Lesselier D, Staraj R (2013) Non-standard antennas, chapter ground-based deformable antennas. Wiley, New York
2. So J-H, Thelen J, Qusba A, Hayes GJ, Lazzi G, Dickey MD (2009) Reversibly deformable and mechanically tunable fluidic antennas. *Adv Funct Mater* 19:36323637
3. Lockyer AJ, Alt KH, Coughlin DP, Durham MD, Kudva JN, Goetz AC, Tuss J (1999) Design and development of a conformal load-bearing smart skin antenna: overview of the AFRL Smart Skin Structures Technology Demonstration (S3TD). In: Jacobs JH (ed) Society of Photo-Optical Instrumentation Engineers (SPIE) Conference Series, vol 3674. Society of Photo-Optical Instrumentation Engineers (SPIE) Conference Series, pp 410–424
4. Volakis JL, Sertel K, Ghosh S (2007) Multiphysics tools for load bearing antennas incorporating novel materials. In: EuCAP 2007—European Conference on Antennas and Propagation, pp. 1–4
5. Ozdemir T, Volakis JL (1997) Triangular prisms for edge-based vector finite element analysis of conformal antennas. *IEEE Trans Antennas Propag* 45(5):788–797
6. Cecot W, Rachowicz W, Demkowicz L (2003) An hp-adaptive finite element method for electromagnetics. Part 3: A three-dimensional infinite element for Maxwell’s equations. *Int J Numer Methods Eng* 57(7):899–921
7. Rachowicz W, Demkowicz L (2002) An hp-adaptive finite element method for electromagnetics. Part ii: A 3D implementation. *Int J Numer Methods Eng* 53(1):147–180
8. Demkowicz L, Kurtz J, Qiu F (2010) hp-adaptive finite elements for coupled multiphysics wave propagation problems. In: *Computer Methods in Mechanics. Advanced Structured Materials*, vol 1. Springer, Berlin, pp. 19–42
9. Semenov AS, Kessler H, Liskowsky A, Balke H (2006) On a vector potential formulation for 3d electromechanical finite element analysis. *Commun Numer Methods Eng* 22(5):357–375
10. Trimarco C (2009) On the dynamics of electromagnetic bodies. *Int J Adv Eng Sci Appl Math* 1:157–162
11. Mota A, Zimmerman JA (2011) A variational, finite-deformation constitutive model for piezoelectric materials. *Int J Numer Methods Eng* 85(6):752–767
12. Thomas JD, Triantafyllidis N (2009) On electromagnetic forming processes in finitely strained solids: theory and examples. *J Mech Phys Solids* 57(8):1391–1416
13. Thomas J, Triantafyllidis N, Vivek A, Daehn G, Bradley J (2010) Comparison of fully coupled modeling and experiments for electromagnetic forming processes in finitely strained solids. *Int J Fract* 163:67–83
14. Pao YH (1978) Electromagnetic forces in deformable continua. *Mech Today* 4(7):1118–1126
15. Zohdi TI (2010) On the dynamics of charged electromagnetic particulate jets. *Arch Comput Methods Eng* 17(2):109–135
16. Zohdi TI (2010) Simulation of coupled microscale multiphysical fields in particulate-doped dielectrics with staggered adaptive ftdtd. *Comput Methods Appl Mech Eng* 199(49–52):3250–3269
17. Zohdi TI (2011) Dynamics of clusters of charged particulates in electromagnetic fields. *Int J Numer Methods Eng* 85(9):1140–1159
18. Zohdi TI (2013) Electromagnetically-induced vibration in particulate-functionalized materials. *J Vib Acoust* 135:8
19. Lax M, Nelson DF (1976) Maxwell equations in material form. *Phys Rev B* 13:1777–1784
20. Trimarco C (2007) Material electromagnetic fields and material forces. *Arch Appl Mech* 77:177–184
21. Zienkiewicz OC, Taylor RL (2000) The finite element method: solid mechanics. *Mecánica y materiales*, vol 2. Butterworth-Heinemann, Oxford
22. Nelson DF (1979) Electric, optic, and acoustic interactions in dielectrics. Wiley, New York
23. Boyse WE, Lynch DR, Paulsen KD, Minerbo GN (1992) Nodal-based finite-element modeling of Maxwell’s equations. *IEEE Trans Antennas Propag* 40(6):642–651
24. Jian Ming J (2002) Finite element method in electromagnetics, 2nd edn. Wiley, New York
25. Polstyanko SV, Dyczij-Edlinger R, Lee JF (1997) Fast frequency sweep technique for the efficient analysis of dielectric waveguides. *IEEE Trans Microw Theory Tech* 45(7):1118–1126
26. Vu-Quoc L, Srinivas V, Zhai Y (2003) Finite element analysis of advanced multilayer capacitors. *Int J Numer Methods Eng* 58(3):397–461
27. Bastos J, Sadowski N (2003) Electromagnetic modeling by finite element methods. Marcel Dekker, New York
28. Subbaraj K, Dokainish MA (1989) A survey of direct time-integration methods in computational structural dynamics-ii. Implicit methods. *Comput Struct* 32(6):1387–1401
29. Karypis G, Schloegel K, Kumar V (2003) ParMETIS parallel graph partitioning and sparse matrix ordering library version 3.1
30. Balay S, Brown J, Buschelman K, Eijkhout V, Gropp WD, Kaushik D, Knepley MG, McInnes LC, Smith BF, Zhang H (2013) PETSc users manual. Technical Report ANL-95/11 - Revision 3.4, Argonne National Laboratory
31. Li Xiaoye S, Demmel James W (2003) SuperLU_DIST: a scalable distributed-memory sparse direct solver for unsymmetric linear systems. *ACM Trans Math Softw* 29(2):110–140
32. COMSOL Multiphysics (2013) Introduction to Comsol Multiphysics, version 4.3b edition
33. ANSYS (2009) Verification manual for the mechanical APDL application, release 12.0 edition
34. Konrad A (1982) Integrodifferential finite element formulation of two-dimensional steady-state skin effect problems. *IEEE Trans Magn* 18(1):284–292
35. Shao K, Zhou K (1985) Transient response in slot-embedded conductor for voltage source solved by boundary element method. *IEEE Trans Magn* 21(6):2257–2260